

A high-resolution spectroscopic search for multiple populations in the 2 Gyr old cluster NGC 1846

W. S. Oh,^{1,2*} T. Nordlander,^{1,2} G. S. Da Costa^{1,2} and A. D. Mackey^{1,2}

¹Research School of Astronomy and Astrophysics, Australian National University, Canberra, ACT 2611

²ARC Centre of Excellence for All Sky Astrophysics in 3 Dimensions (ASTRO 3D), Australia

Accepted XXX. Received YYY; in original form ZZZ

ABSTRACT

We present detailed C, O, Na, Mg, Si, Ca, Ti, V, Fe, Zr, Ba, and Eu abundance measurements for 20 red giant branch (RGB) stars in the LMC star cluster NGC 1846 ([Fe/H] = -0.59). This cluster is 1.95 Gyr old and lies just below the supposed lower age limit (2 Gyr) for the presence of multiple populations in massive star clusters. Our measurements are based on high and low-resolution VLT/FLAMES spectra combined with photometric data from HST. Corrections for non-local thermodynamic equilibrium effects are also included for O, Na, Mg, Si, Ca, Fe and Ba. Our results show that there is no evidence for multiple populations in this cluster based on the lack of any intrinsic star-to-star spread in the abundances of Na and O: we place 95 % confidence limits on the intrinsic dispersion for these elements of ≤ 0.07 and ≤ 0.09 dex, respectively. However, we do detect a significant spread in the carbon abundances, indicating varying evolutionary mixing occurring on the RGB that increases with luminosity. Overall, the general abundance patterns for NGC 1846 are similar to those seen in previous studies of intermediate-age LMC star clusters and field stars.

Key words: Magellanic Clouds – star clusters: individual: NGC 1846 – stars: abundances

1 INTRODUCTION

It has been known for decades that almost every globular cluster (GC) in the Milky Way possesses multiple stellar populations. This refers to a cluster having two main stellar groups: a first generation (1G), consisting of stars that are chemically similar to halo stars, and a second generation (2G), consisting of stars rich in He, N, Na and Al, and poor in C, O and Mg with respect to 1G. (Gratton et al. 2012; Piotto et al. 2015). UV and optical photometric data allows these stellar groups to be differentiated using colour-magnitude diagrams (CMD). Indeed, past studies have shown distinct CMD features for a large number of clusters (~ 60) such as multiple red-giant branches (RGBs), sub-giant branches (SGBs) and even main sequences (MSs) (Milone et al. 2009; Milone et al. 2017), indicating He and N variations (Milone et al. 2018b). These findings have been complemented by spectroscopic observations indicating star-to-star variations in light elements. In particular, they occur in the form of abundance anti-correlations between Na and O, Mg and Al, and C and N (Bastian & Lardo 2018).

However, the origin and mechanism behind these variations are not well understood, since they are not predicted by the basic theory of star cluster formation. Various attempts have been made to explain the production of such abundance patterns, and a popular theory involves the processing of first-generation stellar material at high temperatures, with the processed material then incorporated into a second generation of star formation via a suitable gas reservoir, mixed with some amount of unprocessed material with 1G composition (e.g. D’Ercole et al. 2008; Conroy & Spergel 2011). Examples of

such processing can be found in intermediate-mass asymptotic giant branch (AGB) stars and massive rotating stars. In both cases, enriched material is brought up to the stellar surface where it can be released into the intracluster medium. The mass lost from these stars would form the gas reservoir that is needed to form a second generation of stars with the 2G light-element abundance patterns.

Unfortunately, these and other proposed theories to date have been shown to have at least one fundamental flaw (Renzini et al. 2015; Bastian & Lardo 2018). For example, the two key models (AGB enrichment and fast rotating massive star enrichment) mentioned above both require the formation of multiple generations of stars and hence star formation spanning some extended interval. However, the maximum internal age dispersion observed in young massive star clusters of ~ 30 Myr (De Marchi et al. 2011) is not sufficient for intermediate-mass stars to evolve to the AGB and start polluting the next generation, as this typically takes around 40–160 Myr. On the other hand, this age spread is too large for the small time interval (~ 6 Myr) required between the pollution from massive rotating stars and their supernova explosions (Gratton et al. 2012). Since none of the proposed models have been able to reproduce the main observational properties of multiple stellar populations without making ad hoc assumptions, a self-consistent explanation of the physical processes responsible for the multiple populations phenomenon is lacking, as well as an understanding of which (if any) cluster properties control whether a GC will host chemical anomalies or not (Martocchia et al. 2018; Milone et al. 2019).

Past studies have shown that the role of the estimated initial cluster mass is an important factor in determining whether clusters display multiple populations (Milone et al. 2019). Abundance inhomogeneities are rarely seen in clusters with present-day masses less than

* E-mail: weishen.oh@anu.edu.au

$\sim 10^5$ solar masses (Gratton et al. 2012), which explains why most of the Milky Way clusters that display multiple populations are globular clusters.

Another theory that has been studied in the past is the connection between chemical anomalies and the presence of an extended main-sequence turn-off (eMSTO) in CMDs of star clusters. The eMSTO feature is observed in young and intermediate-age massive clusters (20 Myr - 2 Gyr) (Mackey et al. 2008; Bastian & Lardo 2018; Milone et al. 2018a), and was initially hypothesised to be due to internal age spreads of up to a few hundred Myr, as predicted by some of the previously-discussed models for the formation of light element abundance variations in globular clusters. While multiple populations in GCs have sometimes been inferred purely from the presence of broadened or split main-sequences and turn-offs in the CMDs of young/intermediate-age clusters, these features are not necessarily associated with chemical abundance variations. Recent work by Kamann et al. (2020) (but also see the discussion in Bastian & Lardo 2018) has shown that stellar rotation might be a significant factor in causing features such as the eMSTO to form. Rotation alters the internal stellar structure, because the centrifugal support and extra mixing in the core changes its hydrostatic equilibrium compared to that of a non-rotating star of the same mass and composition. These factors cause the evolutionary path of the rotating star in the CMD to vary in temperature and colour relative to the equivalent non-rotating star. Hence, the relationship with multiple populations in younger clusters (if any) remains unknown.

Therefore, to determine the leading factor for the presence of multiple populations in star clusters, and to better understand the timescale of the multiple population process, one key method is to look for multiple populations in younger populous clusters in nearby galaxies (Gratton et al. 2019), since there are no such clusters in the Milky Way (Portegies Zwart et al. 2010). An example of such objects are the massive intermediate-age (2-8 Gyr) Magellanic Cloud clusters. These are the closest examples of systems with globular cluster-like masses but much younger ages, providing direct snapshots of the cluster formation and evolution process at different times.

Past studies have shown that LMC clusters are also found with an observed splitting or spread in the subgiant and red giant branches when certain photometric filter combinations are used (Martocchia et al. 2018). NGC 2173, with an age of 1.7 Gyr, is the youngest cluster discovered so far that exhibits a split RGB, which is a photometric signature of chemical abundance variations (Kapse et al. 2022). This is one example of a number of works (see Salgado et al. 2022 for further examples) that show that the abundance patterns are not restricted to ancient globular clusters. However, since no spectroscopic analysis of clusters in the LMC younger than 2 Gyr have so far found evidence of chemical abundance spreads (Mucciarelli et al. 2008), we are still unsure of the age dependence for the occurrence of multiple populations in massive clusters.

In this work, we present a high-resolution study of elements including O, Na and Mg in NGC 1846, a LMC massive cluster with a mass of $\sim 6 \times 10^4 M_{\odot}$ (Song et al. 2019) and an age of 1.95 Gyr (Goudfrooij et al. 2009). This will allow a direct test of the 2 Gyr boundary for the age of massive star clusters exhibiting chemical abundance spreads. Compared to UV photometry, our approach allows the chemical abundance variations to be directly determined. In addition, since Na is unaffected by evolutionary mixing unlike in C and N, its abundance variation is a clear indicator of the presence of multiple populations in RGB stars (e.g., Salgado et al. 2022).

We present the observational material for the NGC 1846 RGB stars in Section 2, and our photometric and spectroscopic analysis methods in Section 3. In Section 4, we present results of the abundance

Table 1. Observational setup for the spectroscopic data.

Setting	Wavelength range (Å)	Resolution
HR11	5597–5840	24200
HR13	6120–6405	22500
HR14B	6383–6626	28800
LR02	3964–4567	6000

measurements based on both low and high-resolution spectroscopy. We also analyse the lack of any clear anti-correlation abundance signatures, and present statistical limits on the star-to-star abundance dispersion that may be present.

2 OBSERVATIONS AND DATA REDUCTION

2.1 NGC 1846 RGB stars

The candidate cluster members were selected by Mackey et al. (2013) on the basis of CMD location, distance from the cluster centre and radial velocity. As shown in their Figure 4, there is a well-defined group of candidate members centred on the known cluster velocity of $\sim 240 \text{ km s}^{-1}$ (e.g., ?) and lying within the 161 arcsec truncation radius (Goudfrooij et al. 2009) for the cluster. In contrast, non-members in the same field have radial velocities in the wide range of 210–340 km s^{-1} . Furthermore, Mackey et al. (2013) calculated membership probabilities for the candidates, finding $P_{mem} \gtrsim 99\%$ in most cases; the lowest value is $P_{mem} = 92\%$ for ACS-053 (see their Table 2).

Spectroscopic observations of 20 NGC 1846 RGB stars were obtained during three nights, 2008-11-30, 2008-12-01 and 2008-12-02 under ESO programme 082.D-0387 (PI: Mackey). These were obtained with the FLAMES instrument, which is a fibre-fed multi-object spectrograph mounted on the 8m ESO/VLT telescope. A total of 4 wavelength settings were employed (Table 1), with three high-resolution settings (HR11, HR13, and HR14B) and one low-resolution one (LR02). The RGB stars observed, selected by Mackey et al. (2013) from their HST photometry, are sufficiently bright ($V \leq 19$) that sufficient S/N for high-precision abundance analysis is obtained. The CMD in Figure 1 shows the HST photometry from Mackey et al. (2013) for the NGC 1846 cluster members studied here. The data are well represented by a Dartmouth RGB isochrone assuming literature values for the cluster metallicity and age ([Fe/H] = -0.47 , 1.95 Gyr; Goudfrooij et al. 2009). The lower panels in Figure 1 of Mackey et al. (2013) also show the location of additional stars in the cluster CMD.

We reduced the original raw FLAMES data with the standard ESO GIRAFFE pipeline (esoreflex, version 2.16.7; Blecha et al. 2000). It performs all the basic reduction steps (bias removal, spectrum tracing, flat fielding, and wavelength calibration) together with sky and cosmic-ray subtraction. We did not account for the telluric lines in our spectra as they did not seem to interfere with the abundance measurements of our stars. In the last step, all exposures taken for each star are combined via simple addition to form the final spectra for analysis.¹

¹ As described in Mackey et al. (2013), the observations used the same optical fibre for the same star, and it was found that the change in barycentric correction during the period of observation is negligible.

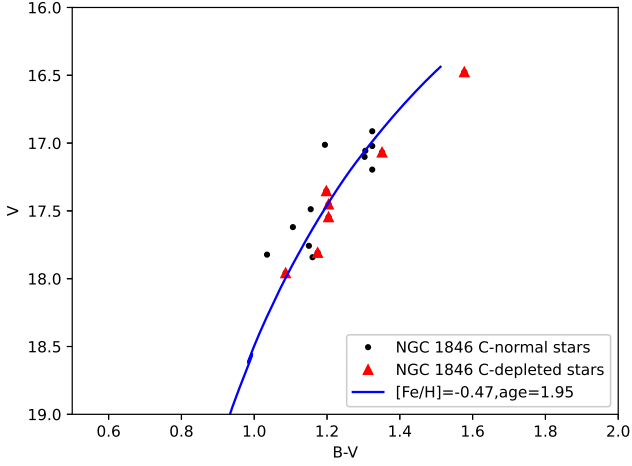


Figure 1. CMD of the NGC 1846 targets using B and V photometry from HST photometry presented by Mackey et al. (2013). ACS-043 and ACS-059 do not have B photometry, hence their values are omitted from the diagram. The red triangles indicate carbon depleted stars while the black points indicate carbon normal stars. This will be discussed in detail in Section 4.2. The Dartmouth RGB isochrone assumes literature values for the metallicity and age ([Fe/H] = -0.47 , 1.95 Gyr; Goudfrooij et al. 2009) has been included for reference.

2.2 Abundance zero-point correction using Arcturus

To obtain a reliable comparison of our measured abundances to the literature values, we must ensure that any systematic effects are accounted for. One way to do this is to apply our methods to the well-studied metal-poor Milky Way giant Arcturus (HD 124 897, α Boo) to obtain a zeropoint for our abundance scale. Since it has similar stellar parameters to the stars in the NGC 1846 sample ($T_{\text{eff}} = 4286$ K, $\log g = 1.66$, [Fe/H] = -0.52) (Ramírez & Allende Prieto 2011) and has also been used in other studies comparing the abundances of LMC stars (Van der Swaelmen et al. 2013), Arcturus is a good choice as a benchmark for our study.

We simulated Arcturus spectra in the four settings (LR02, HR11, HR13 and HR14B) by using the high resolution ($R \sim 150,000$) (Hinkle et al. 2000) spectral atlas of Arcturus. This was degraded according to the resolution required for each setting. The reference Arcturus abundances used are from Ramírez & Allende Prieto (2011) and Worley et al. (2009).

3 PHOTOMETRIC AND SPECTROSCOPIC ANALYSIS METHOD

3.1 Stellar parameters

The surface gravities ($\log g$) for our NGC 1846 sample were derived canonically as shown in Equation (1) below:

$$\log\left(\frac{g}{g_{\odot}}\right) = \log\left(\frac{M}{M_{\odot}}\right) + 4 \log\left(\frac{T_{\text{eff}}}{T_{\odot}}\right) + 0.4(M_{\text{bol}} - M_{\text{bol}\odot}). \quad (1)$$

The steps we took were: Assuming masses of $\sim 1.5M_{\odot}$ for the RGB stars, calculating the bolometric magnitudes using the absorption corrected V magnitudes from HST ($E(B-V) = 0.036$; Mackey et al. 2013), bolometric corrections described in Alonso et al. (1999) and assuming the LMC distance modulus to be 18.52 ± 0.1 mag (Kovacs 2000). The solar bolometric reference value and effective temperature were taken to be 4.74 (Mamajek et al.

Table 2. Stellar parameters for the NGC 1846 RGB stars. Coordinates and photometry are detailed in Mackey et al. 2013.

Name	T_{eff} (K)	$\log g$	[Fe/H]	v_{mic} (km s $^{-1}$)
ACS-001	3940	0.89	-0.63	1.25
ACS-013	4166	1.27	-0.63	1.57
ACS-017	4250	1.42	-0.57	1.61
ACS-025	4291	1.48	-0.59	1.40
ACS-030	4357	1.59	-0.63	1.46
ACS-036	4431	1.72	-0.55	1.54
ACS-043	4462	1.77	-0.52	1.52
ACS-046	4547	1.92	-0.59	0.99
ACS-047	4516	1.86	-0.52	1.30
ACS-053	4534	1.89	-0.68	1.47
ACS-059	4588	1.99	-0.50	1.06
ACS-066	4638	2.08	-0.59	1.38
ACS-080	4212	1.35	-0.62	1.43
ACS-081	4216	1.36	-0.60	1.50
ACS-082	4231	1.38	-0.67	1.45
ACS-085	4236	1.39	-0.61	1.52
ACS-090	4395	1.66	-0.60	1.25
ACS-092	4410	1.68	-0.58	1.32
ACS-102	4540	1.90	-0.61	1.26
ACS-112	4468	1.78	-0.65	1.04

2015) and 5770 K respectively. An initial effective temperature (T_{eff}) estimate was also provided using G–K $_s$ colour-temperature calibrations (using extinction corrected Gaia G and 2MASS K $_s$ magnitudes) from Casagrande et al. (2021).

T_{eff} was then derived by interpolating our $\log g$ values onto a Dartmouth $T_{\text{eff}}-\log g$ isochrone (Dotter et al. 2008) using reddening corrected V magnitudes from HST photometry, assuming literature values for metallicity and age ([Fe/H] = -0.47 , 1.95 Gyr; Goudfrooij et al. 2009).² We tested the G–K $_s$ colour-temperature calibrations as mentioned earlier and found good agreement with our derived temperatures, where our mean bias and standard deviation are 20 K and 90 K respectively. This dispersion is similar to the median uncertainty in T_{eff} from G–K $_s$ (~ 120 K). Given our methodology, it is not straightforward to determine the precision in stellar parameters. To estimate the precision for T_{eff} , we first interpolated the targets' V magnitude using the Dartmouth isochrone (from section 2.1) given a fixed B-V value. The new V magnitude was applied to recalculate the $\log g$ value, which was then used to determine a new T_{eff} value. After which, we derived the offset between the recalculated and the actual T_{eff} values, and its median absolute deviation was found to be 51 K.

Finally, the metallicities and v_{mic} values for the NGC 1846 RGB stars were determined spectroscopically by fitting Fe I & Fe II lines as described in the next section.

3.2 Abundance analysis

3.2.1 High-resolution Abundance analysis

For our spectroscopic analysis, we used the spectrum synthesis code Spectroscopy Made Easy (SME) (version 536) (Piskunov & Valenti 2017) and 1D MARCS model atmospheres (Gustafsson et al. 2008). We implemented NLTE corrections using pre-tabulated grids of departure coefficients for O, Na, Mg, Si, Ca, Ba (Amarsi et al. 2020)

² The values from Goudfrooij et al. (2009) were obtained from fitting the CMD derived from the HST photometry.

and Fe (?). The rest of the elemental abundances were computed assuming LTE. We used atomic and molecular line data from VALD3 (Ryabchikova et al. 2015).

Continuum and line masks were defined mostly by hand, by inspecting a number of spectra to avoid features that appeared too blended or influenced by telluric contamination. The continuum was fitted by dividing the observations by a synthetic spectrum, and fitting a straight line in selected continuum windows. This was done for segments of ~ 50 Å in length. The Fe lines that were used to estimate [Fe/H] were carefully chosen depending on how well the synthetic spectra fit the observed ones. Since the Fe lines found in the HR13 setting were found to be of the best quality amongst all the high-resolution settings, we decided to use the v_{mic} values derived from that setting. As SME performs a global χ^2 fit between synthetic and observed spectra, we determined [Fe/H] individually from each setting and adopted their average as our final metallicity. We chose this approach on the basis that the other elements are located in the various spectrograph settings, and therefore the average Fe value is more representative than using the Fe value from one particular setting. For other elements, we implemented a similar approach to that of Fe. However, a key difference is that in cases where an element could be measured in several settings, we picked the setting that yielded the smallest formal errors.

3.2.2 Low-resolution Abundance analysis

A grid of synthetic spectra were used for our low-res spectroscopic analysis to measure carbon. Spectra were computed as described in Nordlander et al. (2019), using a grid of MARCS model atmospheres (Gustafsson et al. 2008), the synthesis code TurboSpectrum (v15.1; Plez 2012), atomic line data from VALD3 (Ryabchikova et al. 2015) and with molecular data for CH (Masseron et al. 2014) and CN (Brooke et al. 2014; Sneden et al. 2014) as well as numerous other molecules. We adopted a metallicity-dependent alpha enhancement based on typical values in the Milky Way’s disk, $[\alpha/\text{Fe}] = -0.4[\text{Fe}/\text{H}]$, that matches the adopted model atmosphere grid (i.e. $[\alpha/\text{Fe}] \approx 0.2$ at $[\text{Fe}/\text{H}] \approx -0.5$), and computed spectra over a range of v_{mic} , [C/Fe] and [N/Fe] values for each model atmosphere in the grid.

The same stellar parameters were used as for the high-res analysis. We fitted spectra using a χ^2 minimisation, and used a maximum likelihood analysis to ensure detections were significant above the noise level. The continuum and molecular absorption regions were carefully chosen, with the latter being the CH G-band found at ~ 4300 Å. As for nitrogen, we were not able to obtain any reliable abundance measurements as tests on the CN band (4120–4216 Å) showed that it was not possible to provide meaningful constraints on the N abundance.

3.3 Error analysis

We estimated total uncertainties for the abundance measurements by combining statistical and systematic errors. We adopted statistical error estimates from the χ^2 minimisation routine for our high and low-res abundances measurements. Both use the Levenberg-Marquardt χ^2 optimisation and we take σ^2 from the diagonal of the covariance matrix.

The systematic errors are based on uncertainties in the stellar parameters. Due to the high precision in the V magnitudes, the scatter in T_{eff} itself is minimal. Hence, we assume the correlated error between T_{eff} and $\log g$ to be the leading error term, where T_{eff} and $\log g$

Table 3. The chemical composition estimated for Arcturus in this work, reference abundances by (Ramírez & Allende Prieto 2011) (1) and (Worley et al. 2009) (2), and the offsets we applied to match the literature abundance scale.

Element	This work	Literature	Offset	Ref
[C/Fe]	−0.08	0.42	−0.50	1
[O/Fe]	0.50	0.50	0.00	1
[Na/Fe]	0.33	0.11	0.22	1
[Mg/Fe]	0.68	0.37	0.31	1
[Si/Fe]	0.12	0.33	−0.21	1
[Ca/Fe]	0.09	0.11	−0.02	1
[Ti/Fe]	0.26	0.27	−0.01	1
[Fe/H]	−0.73	−0.52	−0.21	1
[V/Fe]	0.25	0.20	0.05	1
[Zr/Fe]	0.13	0.01	0.12	2
[Ba/Fe]	0.06	−0.19	0.25	2
[Eu/Fe]	0.36	0.36	0.00	2

vary in tandem. Taking the error in T_{eff} to be 50 K as described in section 3.1, we find that a shift of 50 K in T_{eff} along the isochrone corresponds to a 0.1 dex change in $\log g$. We note that there is an additional error term in the T_{eff} and $\log g$ scales, due to uncertainties in the adopted reddening, distance modulus, mass and metallicity. But these are comparable to the precision that we derived earlier (~ 0.1 dex for $\log g$ with a correlated 50 K error in T_{eff}), and would have a similar impact on all stars, leading to negligible star-to-star abundance differences. The v_{mic} and [Fe/H] errors were calculated by adopting the standard deviations of the v_{mic} (0.2 km s^{-1}) and [Fe/H] measurements (0.05 dex) respectively. In comparison, we find that perturbing T_{eff} and $\log g$ leads to relatively minor changes in v_{mic} (0.02 km s^{-1}) and [Fe/H] (0.01 dex). These uncertainties were then used to perturb the stellar parameters and compute the change in abundance measurements, which were combined in quadrature to compute the total systematic uncertainty. Finally, the total error was calculated by simply combining the statistical and systematic errors in quadrature.

3.4 Obtaining final abundance measurements

We provide both raw and calibrated abundances. The latter is to account for the systematic trend between the abundance and T_{eff} that occurs for some elements. This is done by fitting a straight line to the measurements and removing the slope while retaining the mean. The slopes are provided in appendix B1 in units of dex/1000K. Finally, offsets were applied to our measured abundances by using the Arcturus abundance measurements to obtain the zero-point corrections for each element. Unless otherwise specified, we will use the calibrated and zero-point corrected abundances in the rest of our analysis.

4 CONSTRAINING THE PRESENCE OF MULTIPLE POPULATIONS IN NGC 1846

In this section, we will present the results showing the lack of evidence for chemical inhomogeneities in Na and O in NGC 1846, indicating there is no evidence for multiple populations present in the cluster. We also present the upper limits for the star-to-star intrinsic abundance scatter for all elements measured.

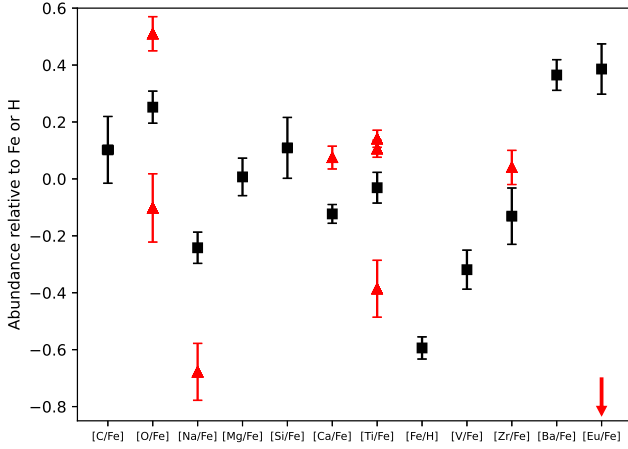


Figure 2. Results of the abundance analysis, represented as a scatter plot, where the black squares indicate the median abundance value and the error bars indicate the median absolute deviation. The red triangles represent outlier points together with their total measurement errors. The outlier for Eu has $[Eu/Fe] = -2 \pm 5$ and is indicated by the red arrow; this is not a genuine detection as indicated by the extremely large error estimate. The outlier stars are: O (ACS-059, ACS-066), Na (ACS-053), Ca (ACS-046), Ti (ACS-001, ACS-066, ACS-112), Zr (ACS-001) and Eu (ACS-059).

4.1 Cluster mean abundances and star-to-star variations

Figure 2 and Table 4 indicate the observed star-to-star spreads and mean abundances respectively for all measured elements. To determine the intrinsic scatter of the abundance measurements that may be hiding beneath the combined errors, we used a Markov Chain Monte Carlo (MCMC) code (Foreman-Mackey et al. 2013) to determine the maximum likelihood value of the intrinsic spread in abundance ratio $[X/Fe]$ for each element. This was done by simulating the total spread in our measurements which combines the statistical, systematic and intrinsic dispersion in quadrature. A uniform prior was adopted. Contour plots were also generated for easier visualization of the data.

Outliers were removed from our data by applying statistical thresholds, which were either if the residual from a straight line fit exceeds 3σ of the residual sample, or if the difference between the abundance and mean exceeds three times of the combined measurement error. We do not know the actual cause of the outliers even after inspecting the respective spectral regions, and they do not appear to be due to systematic errors in stellar parameters. We therefore choose a conservative approach of reporting the status of the outliers, but do not speculate further on the cause.

We have found that the star-to-star dispersion is comparable to the measurement uncertainties for most of the elements, which means that the intrinsic star-to-star spreads for these elements are small (median $\sigma_{\text{int}} \leq 0.04$) as shown in Table 5. The only exceptions are for Zr, Si and C. For Zr and Si, we can attribute this to the relatively large measurement uncertainties based on the standard deviation of the intrinsic abundance dispersion (≥ 0.03), and note that is not unusual for a false positive at the 2 sigma confidence level to arise in a sample of 20 tests. C will be further elaborated in section 4.3.

The abundances of Na and O obtained from our high-res spectroscopy show no sign of any anti-correlation, as shown in Figure 3, which also shows literature data for Milky Way Globular Clusters from Carretta et al. (2009). The formal maximum-likelihood analysis constrains the spreads in O and Na to be $\sigma_{\text{int}} \leq 0.09$ and ≤ 0.07 dex at 95 % confidence, respectively, as shown in Table 5. Corner plots

Table 4. The mean calibrated abundances and the median absolute deviation (MAD) for all elements, plus the spectral regions in which the measured lines occur. The standard error of the mean is also given; systematic errors are not accounted for in these values.

Element	Mean	MAD	Spectral region(s)
[C/Fe]	0.10 ± 0.01	0.12	LR02
[O/Fe]	0.25 ± 0.02	0.06	HR13
[Na/Fe]	-0.24 ± 0.02	0.05	HR13
[Mg/Fe]	0.01 ± 0.02	0.07	HR13
[Si/Fe]	0.11 ± 0.02	0.11	HR13
[Ca/Fe]	-0.12 ± 0.01	0.03	HR14B
[Ti/Fe]	-0.03 ± 0.01	0.05	HR14B
[Fe/H]	-0.59 ± 0.01	0.04	HR11, HR13, HR14B
[V/Fe]	-0.32 ± 0.02	0.07	HR13
[Zr/Fe]	-0.13 ± 0.02	0.10	HR13
[Ba/Fe]	0.37 ± 0.02	0.05	HR13
[Eu/Fe]	0.39 ± 0.03	0.09	HR14B

Table 5. Columns showing the median intrinsic dispersion (σ_{int}), number of stars included in the sample, twice the standard deviation of the intrinsic dispersion ($2\text{SD}(\sigma_{\text{int}})$), and 95 % confidence limit on the maximum σ_{int} for each element measured.

Element	N_{stars}	Median σ_{int}	$2\text{SD}(\sigma_{\text{int}})$	95 % limit on σ_{int}
[C/Fe]	20	0.14	0.05	≤ 0.19
[O/Fe]	18	0.04	0.05	≤ 0.09
[Na/Fe]	19	0.02	0.04	≤ 0.07
[Mg/Fe]	20	0.02	0.03	≤ 0.06
[Si/Fe]	20	0.07	0.08	≤ 0.13
[Ca/Fe]	19	0.02	0.03	≤ 0.05
[Ti/Fe]	17	0.04	0.04	≤ 0.07
[Fe/H]	20	0.02	0.03	≤ 0.05
[V/Fe]	20	0.02	0.04	≤ 0.07
[Zr/Fe]	19	0.05	0.07	≤ 0.12
[Ba/Fe]	20	0.02	0.03	≤ 0.05
[Eu/Fe]	19	0.04	0.06	≤ 0.10

for Na, Mg and O are included in Appendix A1. This confirms that there is no evidence for MPs in NGC 1846.

4.2 Carbon analysis

Our maximum-likelihood analysis indicates that C is the only element that exhibits a robust non-zero star-to-star spread, as shown in the corner plot in Figure 4. While some other elements in the scatter plot (Figure 2) apparently show a comparable spread, their measurement uncertainties are commensurately larger (Refer to Table B2 in the appendix).

To support our finding, we show in Figure 5 a spectral segment in the vicinity of the CH G-band for two NGC 1846 RGB stars (ACS-081 & ACS-082) that have similar stellar parameters but which have significantly different $[C/Fe]$ (values of -0.25 vs 0.20).

We also observe a decreasing C abundance with decreasing $\log(g)$ based on Figure 6, which we interpret as a signature of evolutionary mixing. Potential mixing processes include thermohaline mixing and meridional circulation that occur as stars ascend the RGB, bringing up material from deeper layers that has been processed via thermonuclear CNO burning that converts C into N (Karakas & Lattanzio 2014). However, the spread in our measurements indicates that the degree of mixing varies from star to star, even at similar $\log(g)$. This

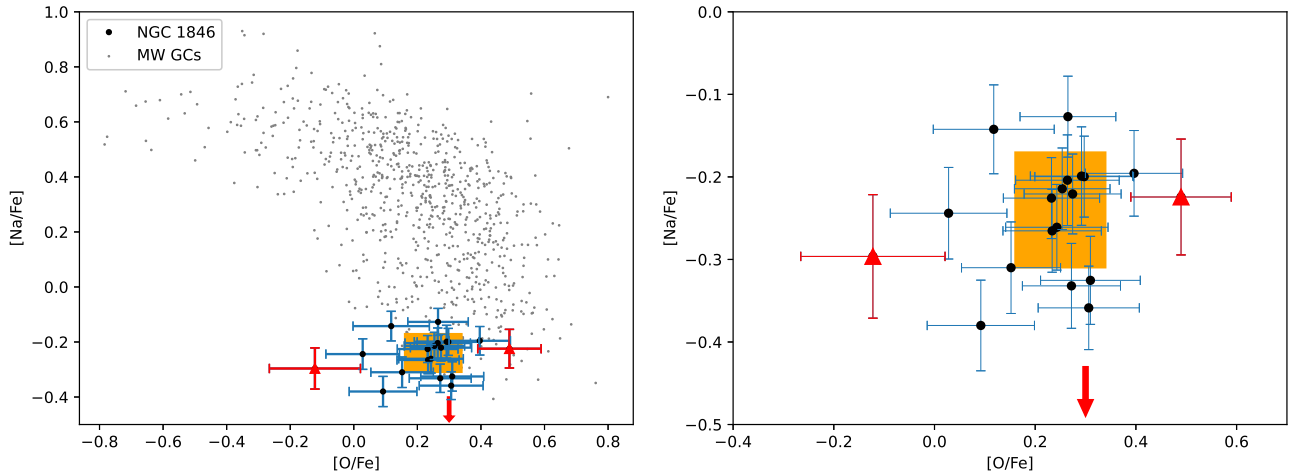


Figure 3. The left plot shows the comparison of the Na and O abundances in the NGC 1846 stars with literature globular cluster values (Carretta et al. 2009). Red triangles indicate the outlier points for O, while the red arrow indicates the outlier point for Na. Error bars denote the combined random and systematic uncertainties associated with each measurement. The orange shaded box covers the central 95 % of the likelihood distribution for the intrinsic spread in Na and O. The right plot shows a zoomed in version of the left plot.

suggests an additional parameter is involved in governing the mixing process.

It is not possible using our available photometry to distinguish whether a star belongs to the RGB or the AGB. Tests with a MIST isochrone indicate that the RGB:AGB ratio in our sample is likely to be 3:1 with an even distribution as a function of $\log g$. It is therefore possible that our most C-depleted stars are AGB, while the rest are RGB. We have marked the most C-depleted stars in Fig. 6 and in the CMD in Fig. 1, which indicates that the C-depleted stars have photometry that is fully compatible with the RGB isochrone. We note in particular that at the luminosities of our stars, AGB stars are double-shell source stars but have not yet reached the regime of third dredge-up where surface carbon abundances increase. Instead, the surface carbon in these stars is expected to be similarly depleted as for our most luminous RGB stars that are approaching the RGB tip.

One possibility is that differences in the rotation velocities of the stars can lead to varying amounts of mixing. Chanamé et al. (2005) predicts that for old field giants, a 30 km s^{-1} difference in initial rotation can lead to 0.5 dex variations in carbon abundance, with stronger rotation leading to stronger depletion, which is similar to what we observe in Figure 6. Moreover, as mentioned in the introduction, Kamann et al. (2020) have shown that the stars in the eMSTO region of NGC 1846 display varying surface rotation rates ($60\text{--}180 \text{ km s}^{-1}$). Inspection of our highest resolution spectra, however, show no indication of surface rotation higher than 10 km s^{-1} in any of our RGB stars. Nevertheless, even though rotation stops on the surface as the star evolves from MS to RGB, it could continue in the core, leading to mixing effects in the upper layers of the star. We note that while Chanamé et al. (2005) only predicted significant depletion of carbon in their rotating models, modern calculations do so even in non-rotating models. As discussed by Karakas & Lattanzio (2014), it is not necessarily true that diffusion coefficients from thermohaline mixing and rotation simply add together – it is possible that rotation actually inhibits thermohaline mixing, and so the effect of rotation on RGB surface abundances may be the opposite of what is discussed above.

Therefore, our results show that it is possible to have a significant intrinsic spread of surface carbon abundance in a cluster without any star-to-star variations in most of the other element abundances

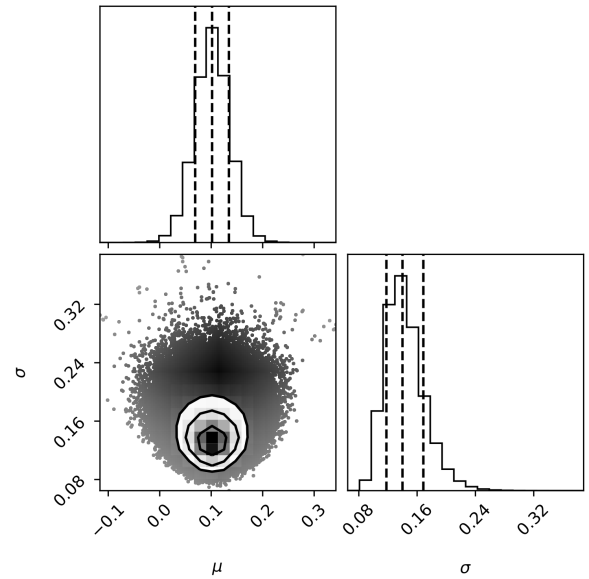


Figure 4. Corner plot showing the mean abundance (μ) and abundance dispersion (σ_{int}) of carbon in NGC 1846. The dashed lines indicate the 25, 50 and 75 percentiles of the intrinsic spread of carbon. The median spread of carbon is 0.140 ± 0.051 .

(including O and Na that are the characteristic signature of MPs in ancient GCs). However, we cannot rule out N variations in our sample. Since hydrogen burning conserves the sum C+N, these stars must also have varying [N/Fe]. These variations may be what has been detected in past photometric surveys of RGB stars. Measuring nitrogen abundances for our sample would thus be an important follow-up project.

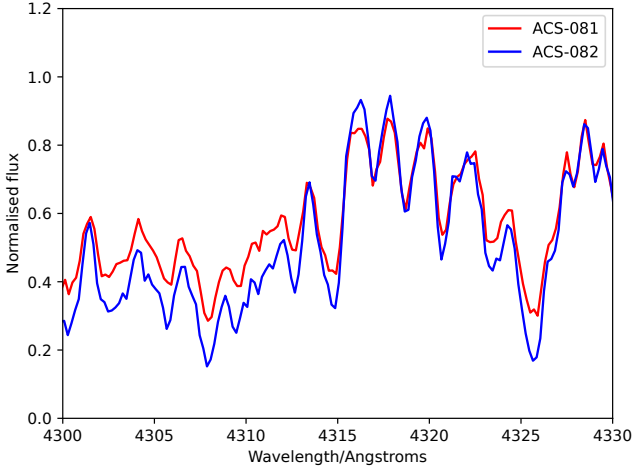


Figure 5. G-band spectral segment showing the difference in CH feature strength for the NGC 1846 RGB stars ACS-081 ($T_{\text{eff}} = 4216$ K) and ACS-082 ($T_{\text{eff}} = 4231$ K). The determined $[C/Fe]$ values from synthetic spectra fits are -0.25 and $+0.20$, respectively.

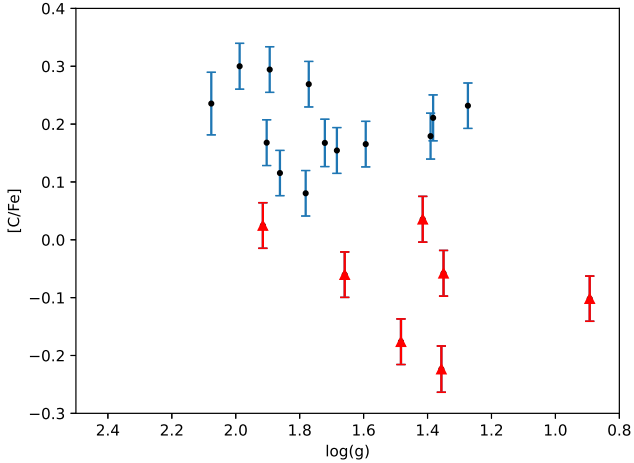


Figure 6. $[C/Fe]$ vs $\log(g)$ plot for the NGC 1846 RGB sample. The red triangles indicate carbon depleted stars while the black points indicate carbon normal stars. The error bars show the combined random and systematic errors of the $[C/Fe]$ abundance measurements for every star.

5 NGC 1846 IN THE LMC CONTEXT

Comparing our abundances for the NGC 1846 sample to past studies of the LMC field stars (bar and inner disc) (Van der Swaelmen et al. 2013) and the LMC intermediate-age cluster stars (Mucciarelli et al. 2008) in Figure 7 and 8, our results indicate that the chemical composition of NGC 1846 is consistent with that of the LMC, resembling more the LMC disc than the bar. This is in line with what we know about NGC 1846, since this cluster is kinematically an LMC disk object³. This also indicates that all the NGC 1846 stars observed are 1G rather than 2G.

Our results also agree with abundances from other LMC

³ The line-of-sight velocity of NGC 1846 ($v_{\text{rad}} \sim 240$ km s⁻¹; Mackey et al. 2013) is comparable with the LMC field’s line-of-sight velocity at the position angle of the cluster with the prediction of disk rotation (van der Marel et al. 2002).

intermediate-age clusters (NGC 1651, 1783, 1978 and 2173), with the exception of V and O. However, our NGC 1846 O abundance measurements interestingly show that they are located in the same region as the bar sample rather than with the disk. This could be due to the NLTE corrections that we used for our O abundance analysis that Van der Swaelmen et al. (2013) did not. In addition, they were only able to measure $[O/Fe]$ in a very small number of disk stars, thus it is unclear if our abundance difference is significant or not.

6 CONCLUSIONS

We present detailed C, O, Na, Mg, Si, Ca, Ti, V, Zr, Ba, and Eu abundance measurements for 20 RGB stars in the LMC star cluster NGC 1846. This cluster is 1.95 Gyr old and lies just below the supposed lower age limit (2 Gyr) for the presence of multiple populations in clusters. Our measurements are based on high and low-resolution VLT/FLAMES spectra combined with photometric data from HST. Corrections for non-local thermodynamic equilibrium effects are also included for O, Na, Mg, Si, Ca, Fe and Ba. Our results show that there is no significant evidence for multiple populations in this cluster based on the lack of star-to-star spread in the Na and O abundances. However, we do detect a significant carbon abundance spread, indicating varying amounts of evolutionary mixing occurring on the RGB. This could be attributed to varying amounts of rotation which alters the amount of mixing from star to star. The general abundance patterns for NGC 1846 are similar to those seen in previous studies of LMC clusters and field stars.

Past studies on multiple populations in intermediate age clusters with similar masses ($\sim 10^5 M_{\odot}$) have found differing results. Mucciarelli et al. (2008) showed using VLT/UVES spectra that 4 of these clusters (NGC 1651, 1783, 1978 and 2173) spanning 1.5 to 2 Gyr in age (Goudfrooij et al. 2014; Martocchia et al. 2018) do not display obvious chemical inhomogeneities. However, in the recent decade, at least two studies have shown that some of these clusters display evidence for MPs. One example is found in the Saracino et al. (2020) study, where Na variations (~ 0.07 dex) have been found using VLT/MUSE spectra in NGC 1978, which has a similar age to NGC 1846. Furthermore, Kapse et al. (2022) recently found that NGC 2173 (~ 1.7 Gyr) also exhibits light-element abundance variations using HST photometry. Therefore, in light of our findings, further high-res spectroscopic analysis is required to confirm the above-mentioned results. Hence, the jury is still out on the extent to which detections of putative multiple populations in younger systems match the variations seen in ancient clusters.

ACKNOWLEDGEMENTS

This paper includes data gathered with the 8m VLT located at Cerro Paranal, Chile, and is based on observations collected at the European Southern Observatory under ESO programme 082.D-0387. ADM acknowledges Australian Research Council grant FT160100206. This research was supported by the Australian Research Council Centre of Excellence for All Sky Astrophysics in 3 Dimensions (ASTRO 3D), through project number CE170100013.

DATA AVAILABILITY

The data used in this study are available in the ESO archive (https://archive.eso.org/eso/eso_archive_main.html) under program ID 082.D-0387. Our coadded spectra are available upon request. The

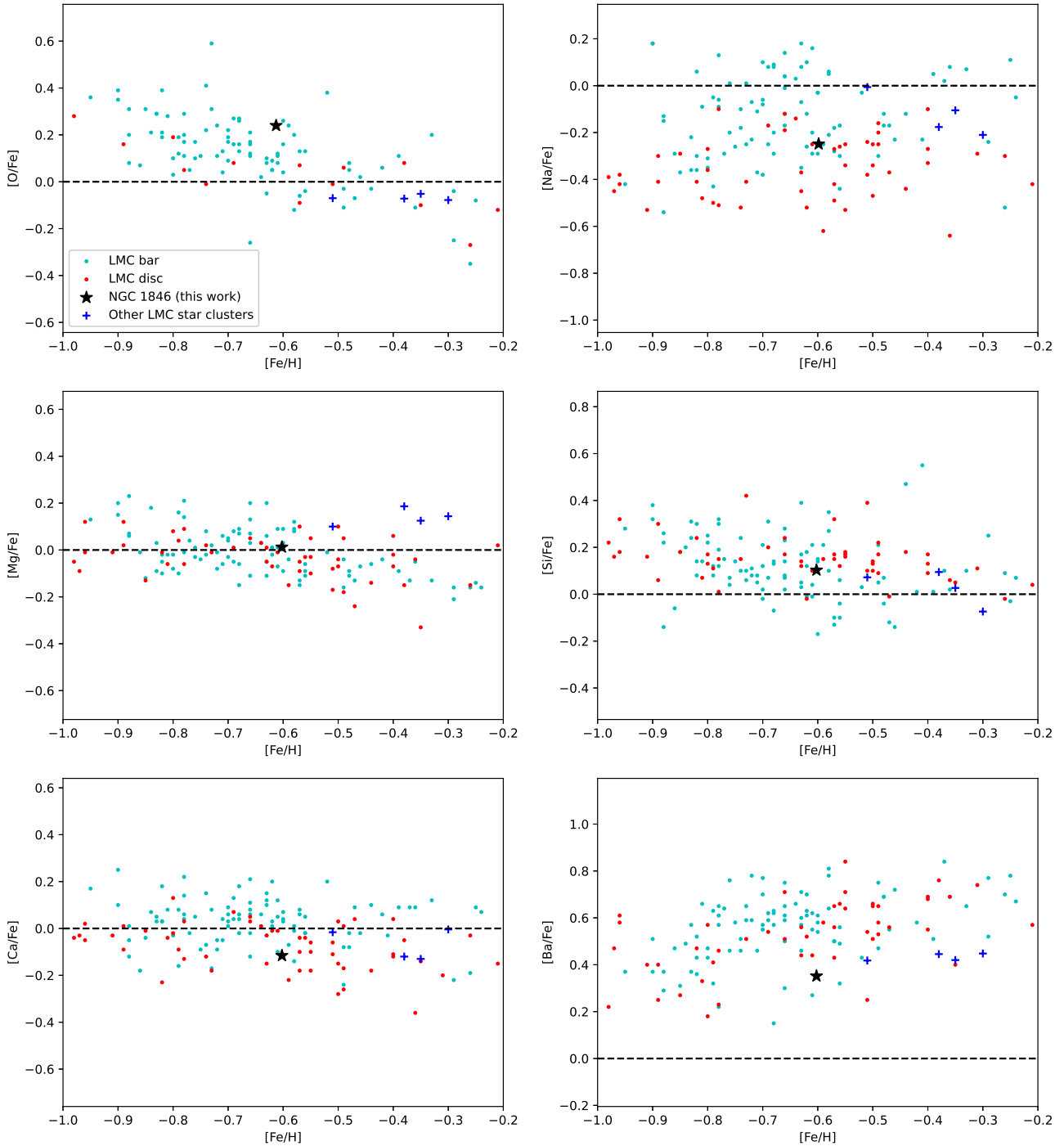


Figure 7. Comparison of our abundances for stars in NGC 1846 (black star) to past studies of LMC field stars (bar - cyan and inner disc - red; [Van der Swaelmen et al. 2013](#)) and for other LMC ~ 2 Gyr old star clusters (blue crosses; [Mucciarelli et al. 2008](#)). Corrections for non-local thermodynamic equilibrium effects were included for these elements. The black dashed line shows the solar abundance level.

ACS/WFC photometric data of NGC 1846 targets only were obtained from [Mackey et al. \(2013\)](#); they originate in HST program GO9891 (PI: Gilmore) and GO10595 (PI: Goudfrooij).

REFERENCES

- Alonso A., Arribas S., Martínez-Roger C., 1999, *Astronomy and Astrophysics Supplement Series*, 140, 261
- Amarsi A. M., et al., 2020, *Astronomy & Astrophysics*, 642, A62
- Bastian N., Lardo C., 2018, *Annual Review of Astronomy and Astrophysics*, 56, 83
- Blecha A., Cayatte V., North P., Royer F., Simond G., 2000, *SPIE*, 4008
- Brooke J. S. A., Ram R. S., Western C. M., Li G., Schwenke D. W., Bernath

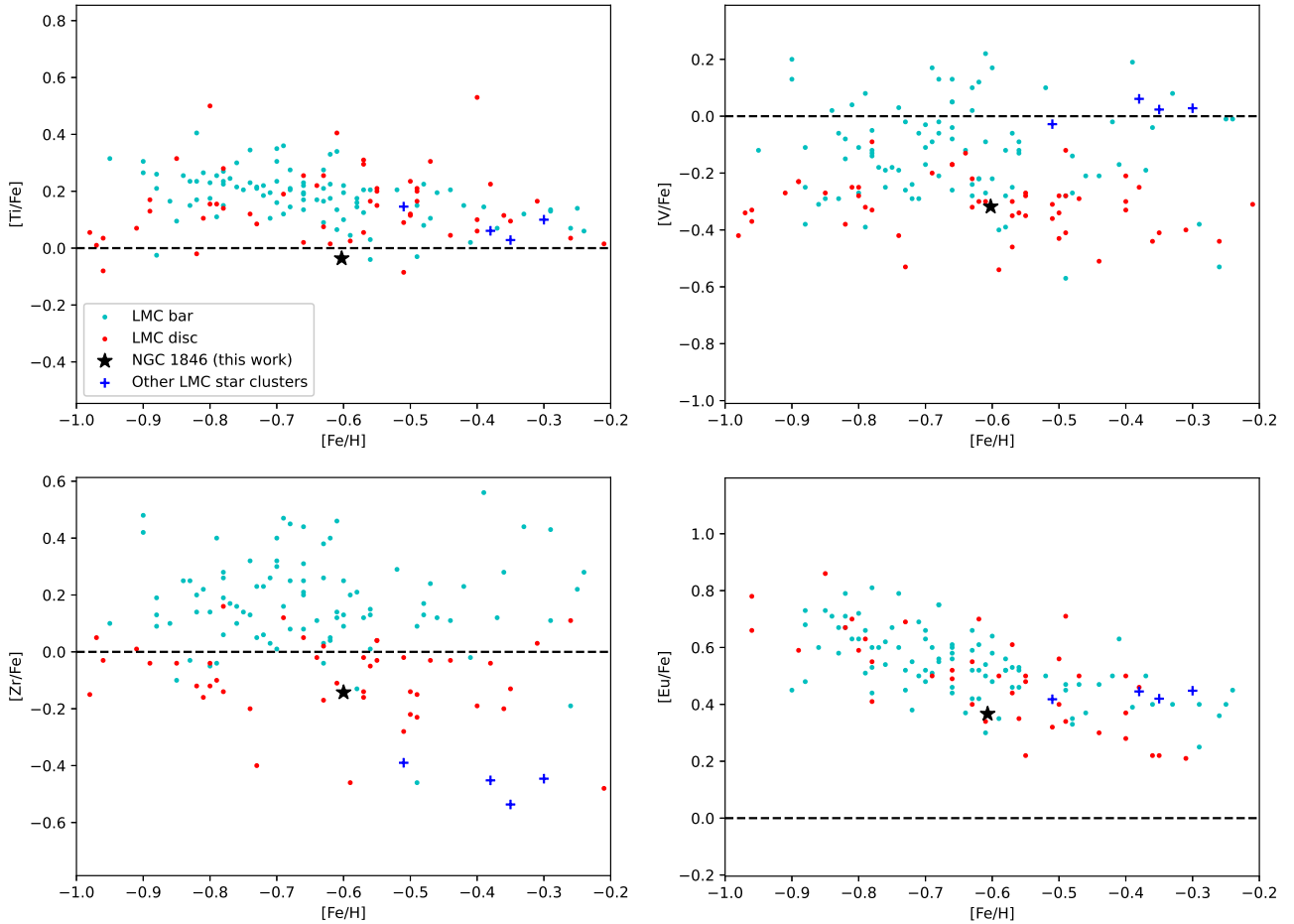


Figure 8. Comparison of our abundances for stars in NGC 1846 (black star) to past studies of LMC field stars (bar - cyan and inner disc - red; Van der Swaelmen et al. 2013) and for other LMC ~ 2 Gyr old star clusters (blue crosses; Mucciarelli et al. 2008). No corrections for non-local thermodynamic equilibrium effects were included for these elements. The black dashed line shows the solar abundance level.

- P. F., 2014, *The Astrophysical Journal Supplement Series*, 210, 23
- Carretta E., et al., 2009, *Astronomy & Astrophysics*, 505, 117
- Casagrande L., et al., 2021, *MNRAS*, 507, 2684
- Chanamé J., Pinsonneault M., Terndrup D. M., 2005, *ApJ*, 631, 540
- Conroy C., Spergel D. N., 2011, *The Astrophysical Journal*, 726, 36
- D’Ercole A., Vesperini E., D’Antona F., McMillan S. L. W., Recchi S., 2008, *Monthly Notices of the Royal Astronomical Society*, 391, 825
- De Marchi G., Panagia N., Sabbi E., 2011, *The Astrophysical Journal*, 740, 10
- Dotter A., Chaboyer B., Jevremović D., Kostov V., Baron E., Ferguson J. W., 2008, *ApJS*, 178, 89
- Foreman-Mackey D., Hogg D. W., Lang D., Goodman J., 2013, *Publications of the Astronomical Society of the Pacific*, 125, 306
- Goudfrooij P., Puzia T. H., Kozhurina-Platais V., Chandar R., 2009, *Astronomical Journal*, 137, 4988
- Goudfrooij P., et al., 2014, *ApJ*, 797, 35
- Gratton R. G., Carretta E., Bragaglia A., 2012, Multiple populations in globular clusters: Lessons learned from the milky way globular clusters ([arXiv:1201.6526](https://arxiv.org/abs/1201.6526)), doi:10.1007/s00159-012-0050-3
- Gratton R., Bragaglia A., Carretta E., D’Orazi V., Lucatello S., Sollima A., 2019, *The Astronomy and Astrophysics Review*, 27, 8
- Gustafsson B., Edvardsson B., Eriksson K., Jørgensen U. G., Nordlund Å., Plez B., 2008, *Astronomy & Astrophysics*, 486, 951
- Hinkle K., Wallace L., Valenti J., Harmer D., 2000, Visible and Near Infrared Atlas of the Arcturus Spectrum 3727-9300 Å. San Francisco: ASP
- Kamann S., et al., 2020, *Monthly Notices of the Royal Astronomical Society*, 492, 2177
- Kapse S., de Grijs R., Kamath D., Zucker D. B., 2022, *The Astrophysical Journal Letters*, 927, L10
- Karakas A. I., Lattanzio J. C., 2014, *Publications of the Astronomical Society of Australia*, 31
- Kovacs G., 2000, *Astronomy and Astrophysics*, 363, 19
- Mackey A. D., Broby Nielsen P., Ferguson A. M. N., Richardson J. C., 2008, *The Astrophysical Journal*, 681, L17
- Mackey A. D., Da Costa G. S., Ferguson A. M., Yong D., 2013, *Astrophysical Journal*, 762
- Mamajek E. E., et al., 2015, IAU 2015 Resolution B2 on Recommended Zero Points for the Absolute and Apparent Bolometric Magnitude Scales, doi:10.48550/ARXIV.1510.06262, <https://arxiv.org/abs/1510.06262>
- Martocchia S., et al., 2018, *Monthly Notices of the Royal Astronomical Society*, 473, 2688
- Masseron T., et al., 2014, *Astronomy and Astrophysics*, 571, A47
- Milone A. P., Bedin L. R., Piotto G., Anderson J., 2009, *Astronomy & Astrophysics*, 497, 755
- Milone A. P., et al., 2017, *Monthly Notices of the Royal Astronomical Society*, 464, 3636
- Milone A. P., et al., 2018a, *Monthly Notices of the Royal Astronomical Society*, 477, 2640
- Milone A. P., et al., 2018b, *MNRAS*, 481, 5098
- Milone A. P., et al., 2019, *Monthly Notices of the Royal Astronomical Society*, 491, 515

Table B1. Slopes of $T_{\text{eff}}\text{-}[X/\text{Fe}]$ for raw abundance measurements for each element.

Element	Slope (dex/1000 K)
[C/Fe]	0.454
[O/Fe]	-0.097
[Na/Fe]	0.027
[Mg/Fe]	-0.022
[Si/Fe]	0.126
[Ca/Fe]	-0.070
[Ti/Fe]	0.022
[Fe/H]	0.146
[V/Fe]	0.010
[Zr/Fe]	-0.170
[Ba/Fe]	-0.136
[Eu/Fe]	-0.290

- Mucciarelli A., Carretta E., Origlia L., Ferraro F. R., 2008, [The Astronomical Journal](#), 136, 375
- Nordlander T., et al., 2019, [Monthly Notices of the Royal Astronomical Society: Letters](#), 488, L109
- Piotto G., et al., 2015, [The Astronomical Journal](#), 149, 91
- Piskunov N., Valenti J. A., 2017, [Astronomy & Astrophysics](#), 597, A16
- Plez B., 2012, Turbospectrum: Code for spectral synthesis, [Astrophysics Source Code Library](#), record ascl:1205.004 (ascl:1205.004)
- Portegies Zwart S. F., McMillan S. L. W., Gieles M., 2010, [ARA&A](#), 48, 431
- Ramírez I., Allende Prieto C., 2011, [The Astrophysical Journal](#), 743, 135
- Renzini A., et al., 2015, [MNRAS](#), 454, 4197
- Ryabchikova T., Piskunov N., Kurucz R. L., Stempels H. C., Heiter U., Pakhomov Y., Barklem P. S., 2015, [Physica Scripta](#), 90, 054005
- Salgado C., Da Costa G. S., Yong D., Salinas R., Norris J. E., Mackey A. D., Marino A. F., Milone A. P., 2022, [MNRAS](#), 515, 2511
- Saracino S., et al., 2020, [MNRAS](#), 498, 4472
- Snedden C., Lucatello S., Ram R. S., Brooke J. S. A., Bernath P., 2014, [The Astrophysical Journal Supplement Series](#), 214, 26
- Song Y.-Y., Mateo M., Mackey A. D., Olszewski E. W., Roederer I. U., Walker M. G., Bailey J. I., 2019, [Monthly Notices of the Royal Astronomical Society](#), 490, 385
- Van der Swaelmen M., Hill V., Primas F., Cole A. A., 2013, [Astronomy & Astrophysics](#), 44, 1
- Worley C. C., Cottrell P. L., Freeman K. C., Wylie-de Boer E. C., 2009, [Monthly Notices of the Royal Astronomical Society](#), 400, 1039
- van der Marel R. P., Alves D. R., Hardy E., Suntzeff N. B., 2002, [AJ](#), 124, 2639

APPENDIX A: ADDITIONAL FIGURES**APPENDIX B: ADDITIONAL TABLES**

We show in Table B1 the slopes of $T_{\text{eff}}\text{-}[X/\text{Fe}]$ for our raw abundance measurements. We applied calibrations to all the raw abundance measurements except for carbon.

In Table B2, we show calibrated abundances of the measured elements. In the online version, we also provide another table with the raw abundances in the same format.

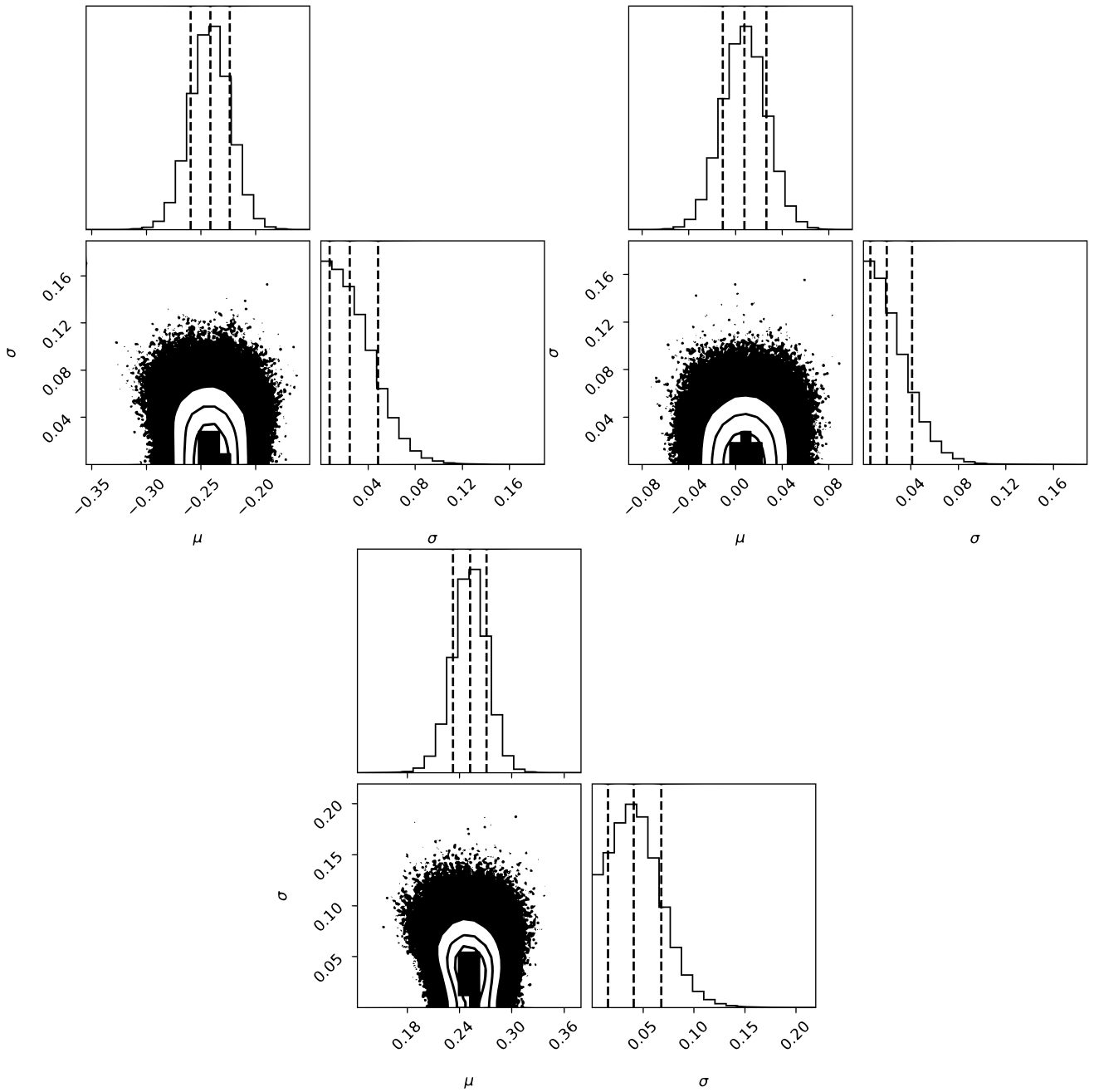


Figure A1. Corner plots showing the mean abundance and abundance dispersion of Na (top-left), Mg (top-right) and O (bottom) in NGC 1846. The dashed lines indicate the 25, 50 and 75 percentiles of the intrinsic spread of the different elements.

Table B2. Abundance table showing the calibrated abundance measurement for each star. The random and systematic errors are given for each element.

Name	[Fe/H] _{calib} [Ca/Fe] _{calib}	[C/Fe] _{calib} [Ti/Fe] _{calib}	[O/Fe] _{calib} [V/Fe] _{calib}	[Na/Fe] _{calib} [Zr/Fe] _{calib}	[Mg/Fe] _{calib} [Ba/Fe] _{calib}	[Si/Fe] _{calib} [Eu/Fe] _{calib}
ACS-001	-0.565 ± 0.008 ± 0.100 -0.059 ± 0.019 ± 0.077	0.094 ± 0.002 ± 0.139 0.106 ± 0.023 ± 0.020	0.112 ± 0.032 ± 0.068 -0.346 ± 0.008 ± 0.062	-0.299 ± 0.031 ± 0.075 0.040 ± 0.025 ± 0.062	-0.053 ± 0.069 ± 0.078 0.400 ± 0.007 ± 0.051	-0.063 ± 0.100 ± 0.085 0.246 ± 0.050 ± 0.062
ACS-013	-0.602 ± 0.008 ± 0.087 -0.218 ± 0.019 ± 0.029	0.325 ± 0.004 ± 0.033 -0.121 ± 0.024 ± 0.037	0.247 ± 0.020 ± 0.057 -0.372 ± 0.005 ± 0.094	-0.122 ± 0.017 ± 0.066 -0.234 ± 0.016 ± 0.092	0.071 ± 0.067 ± 0.070 0.349 ± 0.001 ± 0.083	0.277 ± 0.053 ± 0.067 0.325 ± 0.064 ± 0.055
ACS-017	-0.554 ± 0.012 ± 0.086 -0.063 ± 0.017 ± 0.046	0.091 ± 0.007 ± 0.028 0.039 ± 0.023 ± 0.036	0.223 ± 0.022 ± 0.057 -0.132 ± 0.013 ± 0.094	-0.223 ± 0.017 ± 0.066 0.047 ± 0.017 ± 0.081	-0.027 ± 0.040 ± 0.051 0.380 ± 0.011 ± 0.082	0.102 ± 0.049 ± 0.064 0.312 ± 0.065 ± 0.050
ACS-025	-0.580 ± 0.009 ± 0.077 -0.098 ± 0.020 ± 0.040	-0.140 ± 0.006 ± 0.013 0.062 ± 0.028 ± 0.028	0.292 ± 0.031 ± 0.058 -0.228 ± 0.006 ± 0.103	-0.198 ± 0.017 ± 0.065 0.000 ± 0.018 ± 0.093	0.035 ± 0.061 ± 0.055 0.314 ± 0.013 ± 0.089	0.002 ± 0.067 ± 0.073 0.397 ± 0.062 ± 0.052
ACS-030	-0.631 ± 0.011 ± 0.079 -0.147 ± 0.023 ± 0.040	0.172 ± 0.006 ± 0.031 -0.111 ± 0.036 ± 0.037	0.398 ± 0.026 ± 0.047 -0.367 ± 0.007 ± 0.090	-0.196 ± 0.024 ± 0.00 -0.191 ± 0.030 ± 0.092	0.037 ± 0.050 ± 0.057 0.372 ± 0.015 ± 0.088	0.079 ± 0.061 ± 0.070 0.445 ± 0.078 ± 0.048
ACS-036	-0.555 ± 0.012 ± 0.078 -0.097 ± 0.021 ± 0.037	0.140 ± 0.013 ± 0.044 -0.044 ± 0.035 ± 0.038	0.252 ± 0.041 ± 0.050 -0.285 ± 0.007 ± 0.091	-0.263 ± 0.024 ± 0.066 -0.076 ± 0.026 ± 0.093	-0.057 ± 0.041 ± 0.049 0.281 ± 0.023 ± 0.106	0.043 ± 0.054 ± 0.060 0.409 ± 0.085 ± 0.048
ACS-043	-0.536 ± 0.010 ± 0.086 -0.106 ± 0.025 ± 0.036	0.228 ± 0.005 ± 0.030 0.003 ± 0.035 ± 0.032	0.321 ± 0.034 ± 0.053 -0.244 ± 0.008 ± 0.089	-0.328 ± 0.027 ± 0.073 -0.149 ± 0.037 ± 0.094	-0.011 ± 0.050 ± 0.050 0.294 ± 0.022 ± 0.101	0.085 ± 0.058 ± 0.064 0.359 ± 0.108 ± 0.052
ACS-046	-0.613 ± 0.012 ± 0.087 0.075 ± 0.031 ± 0.028	-0.055 ± 0.006 ± 0.038 0.042 ± 0.041 ± 0.035	0.048 ± 0.069 ± 0.070 -0.394 ± 0.011 ± 0.097	-0.249 ± 0.031 ± 0.074 -0.246 ± 0.081 ± 0.096	0.061 ± 0.057 ± 0.052 0.316 ± 0.020 ± 0.069	0.128 ± 0.083 ± 0.071 0.164 ± 0.200 ± 0.059
ACS-047	-0.541 ± 0.015 ± 0.082 -0.160 ± 0.036 ± 0.041	0.050 ± 0.003 ± 0.077 -0.053 ± 0.057 ± 0.043	0.309 ± 0.041 ± 0.055 -0.264 ± 0.010 ± 0.093	-0.203 ± 0.038 ± 0.067 0.032 ± 0.050 ± 0.090	0.004 ± 0.055 ± 0.047 0.422 ± 0.024 ± 0.068	0.011 ± 0.076 ± 0.067 0.333 ± 0.135 ± 0.049
ACS-053	-0.676 ± 0.014 ± 0.076 -0.117 ± 0.035 ± 0.04	0.221 ± 0.006 ± 0.035 -0.053 ± 0.047 ± 0.046	0.286 ± 0.046 ± 0.047 -0.336 ± 0.012 ± 0.091	-0.673 ± 0.065 ± 0.075 -0.308 ± 0.096 ± 0.096	-0.122 ± 0.068 ± 0.047 0.221 ± 0.046 ± 0.118	-0.004 ± 0.080 ± 0.066 0.337 ± 0.194 ± 0.041
ACS-059	-0.503 ± 0.021 ± 0.081 -0.143 ± 0.051 ± 0.044	0.202 ± 0.007 ± 0.028 -0.029 ± 0.077 ± 0.047	-0.122 ± 0.109 ± 0.064 -0.228 ± 0.013 ± 0.099	-0.296 ± 0.059 ± 0.078 -0.314 ± 0.117 ± 0.107	-0.014 ± 0.060 ± 0.050 0.322 ± 0.037 ± 0.064	0.073 ± 0.097 ± 0.068 -1.460 ± 5.316 ± 0.984
ACS-066	-0.497 ± 0.019 ± 0.081 -0.176 ± 0.047 ± 0.035	0.115 ± 0.038 ± 0.042 -0.381 ± 0.083 ± 0.070	0.490 ± 0.036 ± 0.045 -0.251 ± 0.014 ± 0.104	-0.224 ± 0.053 ± 0.074 0.047 ± 0.063 ± 0.103	0.011 ± 0.089 ± 0.054 0.397 ± 0.031 ± 0.076	-0.206 ± 0.089 ± 0.076 0.299 ± 0.237 ± 0.052
ACS-080	-0.624 ± 0.007 ± 0.091 -0.125 ± 0.017 ± 0.036	0.014 ± 0.006 ± 0.036 0.024 ± 0.022 ± 0.027	0.272 ± 0.029 ± 0.063 -0.327 ± 0.005 ± 0.096	-0.332 ± 0.023 ± 0.079 -0.100 ± 0.019 ± 0.087	0.008 ± 0.046 ± 0.062 0.447 ± 0.012 ± 0.069	0.023 ± 0.053 ± 0.076 0.469 ± 0.051 ± 0.057
ACS-081	-0.599 ± 0.008 ± 0.086 -0.149 ± 0.018 ± 0.039	-0.153 ± 0.009 ± 0.038 -0.038 ± 0.025 ± 0.029	0.274 ± 0.025 ± 0.060 -0.307 ± 0.005 ± 0.090	-0.221 ± 0.015 ± 0.066 -0.119 ± 0.018 ± 0.085	0.010 ± 0.046 ± 0.057 0.383 ± 0.013 ± 0.083	0.038 ± 0.060 ± 0.069 0.503 ± 0.056 ± 0.052
ACS-082	-0.674 ± 0.009 ± 0.08 -0.121 ± 0.022 ± 0.044	0.275 ± 0.007 ± 0.019 -0.068 ± 0.028 ± 0.032	0.254 ± 0.019 ± 0.058 -0.375 ± 0.006 ± 0.094	-0.214 ± 0.018 ± 0.065 -0.121 ± 0.024 ± 0.089	0.059 ± 0.042 ± 0.052 0.283 ± 0.021 ± 0.102	0.242 ± 0.067 ± 0.059 0.570 ± 0.057 ± 0.047
ACS-085	-0.610 ± 0.009 ± 0.083 -0.112 ± 0.022 ± 0.036	0.241 ± 0.007 ± 0.030 -0.058 ± 0.029 ± 0.033	0.306 ± 0.038 ± 0.059 -0.320 ± 0.006 ± 0.099	-0.359 ± 0.021 ± 0.076 -0.186 ± 0.023 ± 0.098	0.121 ± 0.088 ± 0.058 0.319 ± 0.017 ± 0.090	0.251 ± 0.049 ± 0.057 0.340 ± 0.083 ± 0.055
ACS-090	-0.595 ± 0.011 ± 0.082 -0.094 ± 0.025 ± 0.045	-0.071 ± 0.005 ± 0.027 -0.083 ± 0.032 ± 0.037	0.264 ± 0.044 ± 0.053 -0.310 ± 0.007 ± 0.084	-0.204 ± 0.030 ± 0.063 -0.113 ± 0.031 ± 0.086	-0.063 ± 0.042 ± 0.054 0.312 ± 0.016 ± 0.084	0.167 ± 0.065 ± 0.065 0.457 ± 0.072 ± 0.046
ACS-092	-0.575 ± 0.011 ± 0.083 -0.147 ± 0.025 ± 0.035	0.137 ± 0.007 ± 0.032 -0.053 ± 0.040 ± 0.034	0.234 ± 0.030 ± 0.051 -0.409 ± 0.009 ± 0.098	-0.265 ± 0.020 ± 0.073 -0.350 ± 0.040 ± 0.104	-0.096 ± 0.104 ± 0.053 0.389 ± 0.018 ± 0.071	0.176 ± 0.078 ± 0.064 0.254 ± 0.112 ± 0.053
ACS-102	-0.610 ± 0.015 ± 0.079 -0.113 ± 0.034 ± 0.036	0.091 ± 0.007 ± 0.017 -0.075 ± 0.061 ± 0.046	0.118 ± 0.076 ± 0.054 -0.473 ± 0.014 ± 0.099	-0.142 ± 0.028 ± 0.067 -0.213 ± 0.073 ± 0.098	0.091 ± 0.058 ± 0.046 0.405 ± 0.031 ± 0.072	0.271 ± 0.104 ± 0.055 0.416 ± 0.114 ± 0.046
ACS-112	-0.651 ± 0.014 ± 0.082 0.011 ± 0.038 ± 0.049	0.037 ± 0.005 ± 0.050 0.143 ± 0.051 ± 0.027	0.092 ± 0.052 ± 0.051 -0.390 ± 0.012 ± 0.095	-0.380 ± 0.030 ± 0.075 -0.139 ± 0.067 ± 0.089	0.173 ± 0.096 ± 0.056 0.376 ± 0.033 ± 0.061	0.304 ± 0.095 ± 0.052 0.248 ± 0.200 ± 0.049

This paper has been typeset from a $\text{\TeX}/\text{\LaTeX}$ file prepared by the author.